16

Hydrodynamics of a Droplet in Space

Hitoshi Miura
Department of Earth Planetary Materials Science,
Graduate School of Science,
Tohoku University
Japan

1. Introduction

1.1 Droplet in space

It is considered that our solar system 4.6 billion years ago was composed of a proto-sun and the circum-sun gas disk. In the gas disk, originally micron-sized fine dust particles accumulated by mutual collisions to be 1000 km-sized objects like as planets. Therefore, to understand the planet formation, we have to know the evolution of the dust particles in the early solar gas disk. One of the key materials is a millimeter-sized and spherical-shaped grain termed as “chondrule" observed in chondritic meteorites.

Chondrules are considered to have been formed from molten droplets about 4.6 billion years ago in the solar gas disk (Amelin et al., 2002; Amelin & Krot, 2007). Fig. 1 is a schematic of the formation process of chondrules. In the early solar gas disk, aggregation of the micron-sized dust particles took place before planet formation (Nakagawa et al., 1986). When the dust aggregates grew up to about 1 mm in size (precursor), some astrophysical process heated them to the melting point of about $1600 - 2100$ K (Hewins & Radomsky, 1990). The molten dust aggregate became a sphere by the surface tension (droplet), and then cooled again to solidify in a short period of time (chondrule). The formation conditions of chondrules, such as heating duration, maximum temperature, cooling rate, and so forth, have been investigated experimentally by many authors (Blander et al., 1976; Fredriksson & Ringwood, 1963; Harold C. Connolly & Hewins, 1995; Jones & Lofgren, 1993; Lofgren & Russell, 1986; Nagashima et al., 2006; Nelson et al., 1972; Radomsky & Hewins, 1990; Srivastava et al., 2010; Tsuchiyama & Nagahara, 1981-12; Tsuchiyama et al., 1980; 2004; Tsukamoto et al., 1999). However, it has been controversial what kind of astronomical event could have produced chondrules in early solar system. The chondrule formation is one of the most serious unsolved problems in planetary science.

The most plausible model for chondrule formation is a shock-wave heating model, which has been tested by many theoreticians (Ciesla & Hood, 2002; Ciesla et al., 2004; Desch & Jr., 2002; Hood, 1998; Hood & Horanyi, 1991; 1993; Iida et al., 2001; Miura & Nakamoto, 2006; Miura et al., 2002; Morris & Desch, 2010; Morris et al., 2009; Ruzmaikina & Ip, 1994; Wood, 1984). Fig. 2 is a schematic of dust heating mechanism by the shock-wave heating model. Initially, the chondrule precursors were floating in the gas disk without any large relative velocity against the ambient gas (panel (a)). When a shock wave was generated in the gas disk, the gas behind the shock front was accelerated suddenly. On the other hand, the chondrule

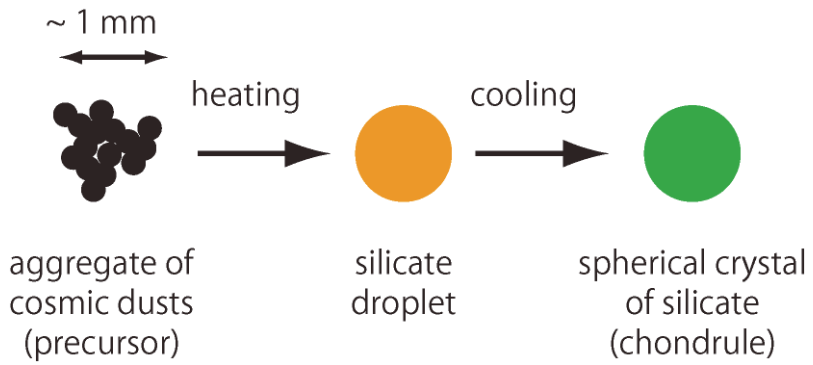

Fig. 1. Schematic of formation process of a chondrule. The precursor of chondrule is an aggregate of μm-sized cosmic dusts. The precursor is heated and melted by some mechanism, becomes a sphere by the surface tension, then cools to solidify in a short period of time.

precursors remain un-accelerated because of their inertia. Therefore, after passage of the shock front, the large relative velocity arises between the gas and dust particles (panel (b)). The relative velocity can be considered as fast as about 10 km s^{-1} (Iida et al., 2001). When the gas molecule collides to the surface of chondrule precursors with such large velocity, its kinetic energy thermalizes at the surface and heats the chondrule precursors, as termed as a gas drag heating. The peak temperature of the precursor is determined by the balance between the gas drag heating and the radiative cooling at the precursor surface (Iida et al., 2001). The gas drag heating is capable to heat the chondrule precursors up to the melting point if we consider a standard model of the early solar gas disk (Iida et al., 2001).

1.2 Physical properties of chondrules

The chondrule formation models, including the shock-wave heating model, are required not only to heat the chondrule precursors up to the melting point but also to reproduce other physical and chemical properties of chondrules recognized by observations and experiments. These properties that should be reproduced are summarized as observational constraints (Jones et al., 2000). The reference listed 14 constraints for chondrule formation. To date, there is no chondrule formation model that can account for all of these constraints.

Here, we review two physical properties of chondrules; size distribution and three-dimensional shape. The latter was not listed as the observational constraints in the literature (Jones et al., 2000), however, we would like to include it as an important constraint for chondrule formation. As discussed in this chapter, these two properties strongly relate to the hydrodynamics of molten chondrule precursors in the gas flow behind the shock front.

1.2.1 Size distribution

Fig. 3 shows the size distribution of chondrules compiled from measurement data in some literatures (Nelson & Rubin, 2002; Rubin, 1989; Rubin & Grossman, 1987; Rubin & Keil, 1984). The horizontal axis is the diameter D and the vertical axis is the cumulative fraction of

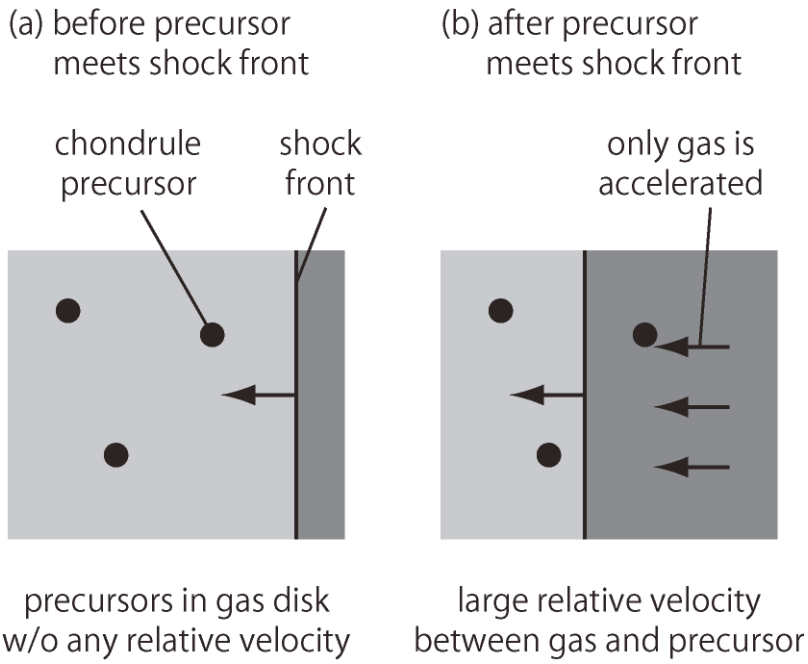

Fig. 2. Schematic of the shock-wave heating model for chondrule formation. (a) The precursors of chondrules are in a gas disk around the proto-sun 4.6 billion years ago. The gas and precursors rotate around the proto-sun with almost the same angular velocity, so there is almost no relative velocity between the gas and precursors. (b) If a shock wave is generated in the gas disk by some mechanism, the gas behind the shock front is suddenly accelerated. In contrast, the precursor is not accelerated because of its large inertia. The difference of their behaviors against the shock front causes a large relative velocity between them. The precursors are heated by the gas friction in the high velocity gas flow.

chondrules smaller than D in diameter. Table 1 shows the mean diameter and the standard deviation of each measurement. It is found that the chondrule sizes vary according to chondrite type. The mean diameters of chondrules in ordinary chondrites (LL3 and L3) are from 600 μm to 1000 μm. In contrast, ones in enstatite chondrite (EH3) and carbonaceous chondrite (CO3) are from 100 μm to 200 μm.

It should be noted that the true chondrule diameters are slightly larger than the data shown in Fig. 3 and Table 1 because of the following reason. This data was obtained by observations on thin-sections of chondritic meteorites. The chondrule diameter on the thin-section is not necessarily the same as the true one because the thin-section does not always intersect the center of the chondrule. Statistically, the mean and median diameters measured on the thin section are, respectively, $\sqrt{2}/3$ and $\sqrt{3}/4$ of the true diameters (Hughes, 1978). However, we do not take care the difference between true and measured diameters because it is not a substantial issue in this chapter.

It is considered that in the early solar gas disk the dust aggregates have the size distribution from $\approx$ μm (initial fine dust particles) to a few 1000 km (planets). In spite of the wide

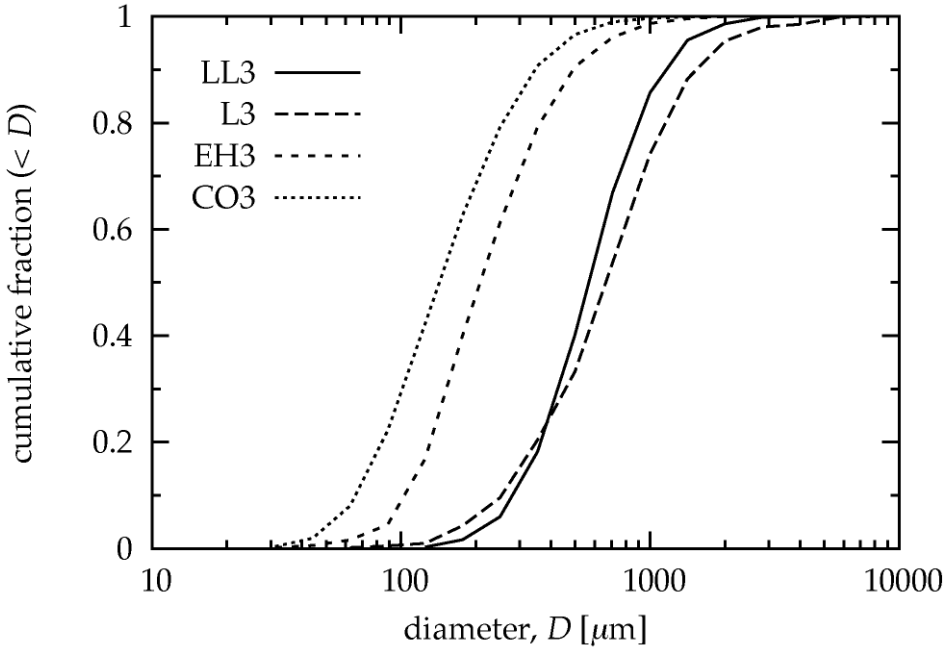

Fig. 3. Size distributions of natural chondrules in various types of chondritic meteorites (LL3, L3, EH3, and CO3). The vertical axis is the normalized cumulative number of chondrules whose diameters are smaller than that of the horizontal axis. Each data was compiled from the following literatures; LL3 chondrites (Nelson & Rubin, 2002), L3 chondrites (Rubin & Keil, 1984), EH3 chondrites (Rubin & Grossman, 1987), and CO3 chondrites (Rubin, 1989), respectively. The total number of chondrules measured in each literature is 719 for LL3, 607 for L3, 689 for EH3, and 2834 for CO3, respectively.

size range of solid materials, sizes of chondrules distribute in a very narrow range of about $100 - 1000$ μm. Two possibilities for the origin of chondrule size distribution can be considered; (i) size-sorting prior to chondrule formation, and (ii) size selection during chondrule formation. In the case of (i), we need some mechanism of size-sorting in the early solar gas disk (Teitler et al., 2010, and references therein). In the case of (ii), the chondrule formation model must account for the chondrule size distribution. The latter possibility is what we investigate in this chapter.

1.2.2 Deformation from a perfect sphere

It is considered that spherical chondrule shapes were due to the surface tension when they melted. However, their shapes deviate from a perfect sphere and the deviation is an important clue to identify the formation mechanism. Tsuchiyama et al. (Tsuchiyama et al., 2003) measured the three-dimensional shapes of chondrules using X-ray microtomography. They selected 20 chondrules with perfect shapes and smooth surfaces from 47 ones for further analysis. Their external shapes were approximated as three-axial ellipsoids with axial radii of a, b, and c ($a \geq b \geq c$), respectively. Fig. 4 shows results of the measurement. The horizontal

chondrite type	meteorite type	chondrule type*	number	diam. D [μm]	ref.
L3	Inman	BO	173	1038±937	(Rubin & Keil, 1984)
L3	Inman	RP+C	201	852±598	(Rubin & Keil, 1984)
L3	ALHA77011	BO	163	680±625	(Rubin & Keil, 1984)
L3	ALHA77011	RP+C	70	622±453	(Rubin & Keil, 1984)
LL3	total of 5 types	all	719	574^{+405}_{-237}	(Nelson & Rubin, 2002)
EH3	total of 3 types	all	689	219^{+189}_{-101}	(Rubin & Grossman, 1987)
CO3	total of 11 types	all	2834	148^{+132}_{-70}	(Rubin, 1989)

Table 1. Diameters of chondrules from various types of chondritic meteorites and the standard deviations. *BO = barred olivine, RP = radial pyroxene, C = cryptocrystalline. all = all types are included.

and vertical axes are axial ratios of b/a and c/b, respectively. A point $(b/a, c/b) = (1, 1)$ means a perfect sphere because all of three axes have the same length. As going downward from the point, the shape becomes oblate (disk-like shape) because $a = b > c$. On the other hand, the shape becomes prolate (rugby-ball-like shape) as going leftward because $a > b = c$. The chondrule shapes in the measurement are classified into two groups: spherical chondrules in group-A and prolate chondrules in group-B. Chondrules in group-A have axial ratios of $c/b >\sim 0.9$ and $b/a >\sim 0.9$. In contrast, chondrules in group-B have smaller values of b/a as $\approx 0.7 - 0.8$.

It is considered that the deviation from a perfect sphere results from the deformation of a molten chondrule before solidification. For example, if the molten chondrule rotates rapidly, the shape becomes oblate due to the centrifugal force (Chandrasekhar, 1965). However, the shapes of chondrules in group-B are prolate rather than oblate. Tsuchiyama et al. (Tsuchiyama et al., 2003) proposed that the prolate chondrules in group-B can be explained by spitted droplets due to the shape instability with high-speed rotation. However, it is not clear whether the transient process such as the shape instability accounts for the range of axial ratio of group-B chondrules or not.

1.3 Hydrodynamics of molten chondrule precursors

If chondrules were melted behind the shock front, the molten droplet ought to be exposed to the high-velocity gas flow. The gas flow causes many hydrodynamics phenomena on the molten chondrule droplet as follows. (i) Deformation: the ram pressure deforms the droplet shape from a sphere. (ii) Internal flow: the shearing stress at the droplet surface causes fluid flow inside the droplet. (iii) Fragmentation: a strong gas flow will break the droplet into many tiny fragments. Hydrodynamics of the droplet in high-velocity gas flow strongly relates to the physical properties of chondrules. However, these hydrodynamics behaviors have not been investigated in the framework of the chondrule formation except of a few examples that neglected non-linear effects of hydrodynamics (Kato et al., 2006; Sekiya et al., 2003; Uesugi et al., 2005; 2003).

To investigate the hydrodynamics of a molten chondrule droplet in the high-velocity gas flow, we performed computational fluid dynamics (CFD) simulations based on cubic-interpolated propagation/constrained interpolation profile (CIP) method. The CIP method is one of the high-accurate numerical methods for solving the advection equation (Yabe & Aoki, 1991;

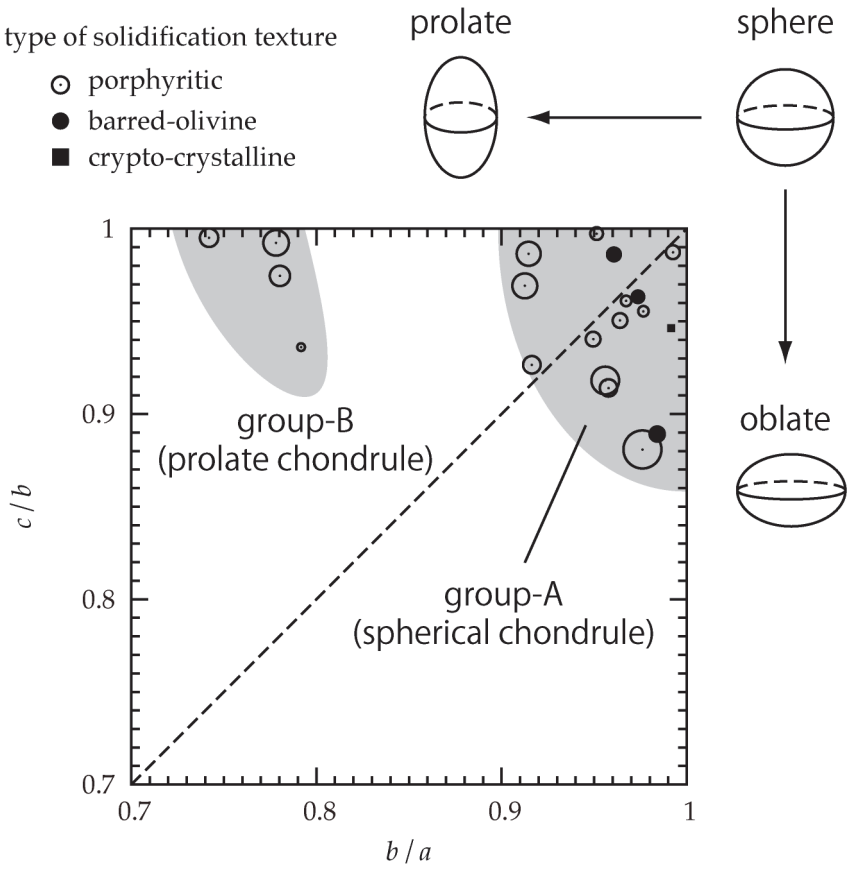

Fig. 4. Three-dimensional shapes of chondrules (Tsuchiyama et al., 2003, and their unpublished data). a, b, and c are axial radii of chondrules when their shapes are approximated as three-axial ellipsoids ($a \geq b \geq c$), respectively. The textures of these chondrules are 16 porphyritic (open circle), 3 barred-olivine (filed circle), and 1 crypto-crystalline (filled square). The radius of each symbol is proportional to the effective radius of each chondrule $r_* \equiv (abc)^{1/3}$; the largest circle corresponds to $r_* = 1129$ ¯m. For the data of crypto-crystalline, $r_* = 231$ ¯m. Chondrule shapes are classified into two groups: group-A shows the relatively small deformation from the perfect sphere, and group-B is prolate with axial ratio of $b/a \approx 0.7 - 0.8$.

Yabe et al., 2001). It can treat both compressible and incompressible fluids with large density ratios simultaneously in one program (Yabe & Wang, 1991). The latter advantage is important for our purpose because the droplet density ($\approx$ 3 g cm^{-3}) differs from that of the gas disk ($\approx 10^{-8}$ g cm^{-3} or smaller) by many orders of magnitude.

In addition, we should pay a special attention how to model the ram pressure of the gas flow. The gas around the droplet is so rarefied that the mean free path of the gas molecules is an order of about 100 cm if we consider a standard gas disk model. The mean free path is much larger than the typical size of chondrules. This means that the gas flow around the droplet is a free molecular flow, so it does not follow the hydrodynamical equations. Therefore, in our model, the ram pressure acting on the droplet surface per unit area is explicitly given in the equation of motion for the droplet by adopting the momentum flux method as described in section 3.2.2.

1.4 Aim of this chapter

The hydrodynamical behaviors of molten chondrules in a high-velocity gas flow are important to elucidate the origin of physical properties of chondrules. However, it is difficult for experimental studies to simulate the high-velocity gas flow in the early solar gas disk, where the gas density is so rarefied that the gas flow around droplets does not follow the hydrodynamics equations. We developed the numerical code to simulate the droplet in a high-velocity rarefied gas flow. In this chapter, we describe the details of our hydrodynamics code and the results. We propose new possibilities for the origins of size distribution and three-dimensional shapes of chondrules based on the hydrodynamics simulations.

We describe the governing equations in section 2 and the numerical procedures in section 3. In section 4, we describe the results of the hydrodynamics simulations regarding the deformation of molten chondrules in the high-velocity rarefied gas flow and discuss the origin of rugby-ball-like shaped chondrules. In section 5, we describe the results regarding the fragmentation of molten chondrules and consider the relation to the size distribution of chondrules. We conclude our hydrodynamics simulations in section 6.

2. Governing equations

The governing equations are the equation of continuity and the Navier-Stokes equation as follows;

$$\frac{\partial \rho}{\partial t} + \vec{\nabla} \cdot (\rho \vec{u}) = 0, \tag{1}$$

$$\frac{\partial \vec{u}}{\partial t} + (\vec{u} \cdot \vec{\nabla})\vec{u} = \frac{-\vec{\nabla} p + \mu \nabla^2 \vec{u} + \vec{F}_{\mathrm{s}} + \vec{F}_{\mathrm{g}}}{\rho} + \vec{g}, \tag{2}$$

where ρ is the density of fluid, $\vec{u}$ is the velocity, p is the pressure, and μ is the viscosity. The ram pressure of the high-velocity gas flow, $\vec{F}_{\mathrm{g}}$, is exerted on the surface of the droplet and given by (Sekiya et al., 2003)

$$\vec{F}_{\mathrm{g}} = -p_{\mathrm{fm}} (\vec{n}_{\mathrm{i}} \cdot \vec{n}_{\mathrm{g}}) \vec{n}_{\mathrm{g}} \delta(\vec{r} - \vec{r}_{\mathrm{i}}) \quad \text{for } \vec{n}_{\mathrm{i}} \cdot \vec{n}_{\mathrm{g}} \leq 0, \tag{3}$$

where $\vec{n}_{\mathrm{i}}$ is the unit normal vector of the surface of the droplet, $\vec{n}_{\mathrm{g}}$ is the unit vector pointing the direction in which the gas flows, and $\vec{r}_{\mathrm{i}}$ is the position of the liquid-gas interface. The delta function $\delta(\vec{r} - \vec{r}_{\mathrm{i}})$ means that the ram pressure works only at the interface. The ram

pressure does not work for $\vec{n}_i \cdot \vec{n}_g > 0$ because it indicates the opposite surface which does not face the molecular flow. The ram pressure causes the deceleration of the center of mass of the droplet. In our coordinate system co-moving with the center of mass, the apparent gravitational acceleration $\vec{g}$ should appear in the equation of motion. The surface tension, $\vec{F}_s$, is given by (Brackbill et al., 1992)

$$\vec{F}_s = -\gamma_s \kappa \vec{n}_i \delta(\vec{r} - \vec{r}_i), \tag{4}$$

where γ_s is the fluid surface tension and κ is the local surface curvature. Finally, we consider the equation of state given by

$$\frac{dp}{d\rho} = c_s^2, \tag{5}$$

where c_s is the sound speed.

3. Numerical methods in hydrodynamics

To solve the equation of continuity (Eq. (1)) numerically, we introduce a color function ϕ that changes from 0 to 1 continuously. For incompressible two fluids, a density in each fluid is uniform and has a sharp discontinuity at the interface between these two fluids if the density of a fluid is different from another one. By using the color function, we can distinguish these two fluids as follows; $\phi = 1$ for fluid 1, $\phi = 0$ for fluid 2, and a region where $0 < \phi < 1$ for the interface. The density of a fluid element is given by

$$\rho = \phi\rho_1 + (1 - \phi)\rho_2, \tag{6}$$

where ρ_1 and ρ_2 are the inherent densities for fluid 1 and fluid 2, respectively. The governing equation for ϕ is given by

$$\frac{\partial \phi}{\partial t} + \vec{\nabla} \cdot (\phi \vec{u}) = 0. \tag{7}$$

The conservation equation for ϕ (Eq. (7)) is approximately equivalent to the original one (Eq. (1)) through the relationship between ρ and ϕ given by Eq. (6) (Miura & Nakamoto, 2007). Therefore, the problem to solve Eq. (1) results in to solve Eq. (7). We solve Eq. (7) using R-CIP-CSL2 method with anti-diffusion technique (sections 3.1.2 and 3.1.3).

In this study, the fluid 1 is the molten chondrule and the fluid 2 is the disk gas around the chondrule. The inherent densities are given by $\rho_1 = \rho_d$ and $\rho_2 = \rho_a$, where subscripts "d" and "a" mean the droplet and ambient gas, respectively. The other physical values of the fluid element (viscosity μ and sound speed c_s) are given in the same manner as the density ρ, namely, $\mu = \phi\mu_d + (1 - \phi)\mu_a$ and $c_s = \phi c_{s,d} + (1 - \phi)c_{s,a}$, respectively.

The Navier-Stokes equation (Eq. (2)) and the equation of state (Eq. (5)) are separated into two phases; the advection phase and the non-advection phase. The advection phases are written as

$$\begin{aligned} \frac{\partial \vec{u}}{\partial t} + (\vec{u} \cdot \vec{\nabla})\vec{u} &= 0, \\ \frac{\partial p}{\partial t} + (\vec{u} \cdot \vec{\nabla})p &= 0. \end{aligned} \tag{8}$$

Parameter	Sign	Value
Momentum of gas flow	p_{fm}	4000 dyn cm^{-2}
Surface tension	γ_{s}	400 dyn cm^{-1}
Viscosity of droplet	μ_{d}	1.3 g cm^{-1} s^{-1}
Density of droplet	ρ_{d}	3 g cm^{-3}
Sound speed of droplet	$c_{\mathrm{s,d}}$	2×10^{5} cm s^{-1}
Density of ambient	ρ_{a}	10^{-6} g cm^{-3}
Sound speed of ambient	$c_{\mathrm{s,a}}$	10^{-5} cm s^{-1}
Viscosity of ambient	μ_{a}	10^{-2} g cm^{-1} s^{-1}
Droplet radius	r_0	500 μm

Table 2. Canonical input physical parameters for simulations of molten chondrules exposed to the high-velocity rarefied gas flow. We ought to use these parameters if there is no special description.

We solve above equations using the R-CIP method, which is the oscillation preventing method for advection equation (section 3.1.1). The non-advection phases can be written as

$$\begin{aligned}\frac{\partial \vec{u}}{\partial t} &= -\frac{\vec{\nabla} p}{\rho} + \frac{\vec{Q}}{\rho},\\ \frac{\partial p}{\partial t} &= -\rho c_{\mathrm{s}}^2 \vec{\nabla}\cdot\vec{u},\end{aligned} \tag{9}$$

where $\vec{Q}$ is the summation of forces except for the pressure gradient. The problem intrinsic in incompressible fluid is in the high sound speed in the pressure equation. Yabe and Wang (Yabe & Wang, 1991) introduced an excellent approach to avoid the problem (section 3.2.1). It is called as the C-CUP method (Yabe & Wang, 1991). The numerical methods to calculate ram pressure of the gas flow and the surface tension of droplet in $\vec{Q}$ are described in sections 3.2.2 and 3.2.3, respectively.

The input parameters adopted in this chapter are listed in Table 2.

3.1 Advection phase

3.1.1 CIP method

The CIP method is one of the high-accurate numerical methods for solving the advection equation (Yabe & Aoki, 1991; Yabe et al., 2001). In one-dimension, the advection equation is written as

$$\frac{\partial f}{\partial t} + u\frac{\partial f}{\partial x} = 0, \tag{10}$$

where f is a scaler variable of the fluid (e.g., density), u is the fluid velocity in the x-direction, and t is the time. When the velocity u is constant, the exact solution of Eq. (10) is given by

$$f(x;t) = f(x-ut;0), \quad \text{when } u \text{ is constant}, \tag{11}$$

which indicates a simple translational motion of the spatial profile of f with the constant velocity u.

Let us consider that the values of f on the computational grid points x_{i-1}, x_i, and x_{i+1} are given at the time step n and denoted by f_{i-1}^n, f_i^n, and f_{i+1}^n, respectively. In Fig. 5, f^n are shown

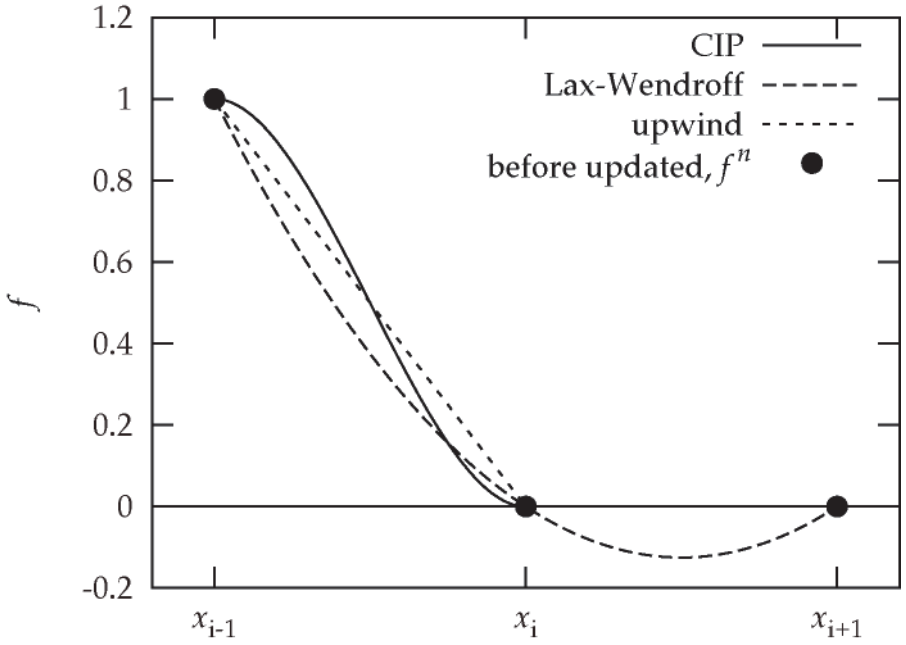

Fig. 5. Interpolate functions with various methods: CIP (solid), Lax-Wendroff (dashed), and first-order upwind (dotted). The filled circles indicate the values of f defined on the digitized grid points x_{i-1}, x_i, and x_{i+1} before updated.

by filled circles. From Eq. (11), we can obtain the values of f_i at the next time step $n+1$ by just obtaining f_i^n at the upstream point $x = x_i - u\Delta t$, where Δt is the time interval between t^n and t^{n+1}. If the upstream point is not exactly on the grid points, which is a very usual case, we have to interpolate f_i^n with an appropriate mathematical function composed of f_{i-1}^n, f_i^n, and so forth. There are some variations of the numerical solvers by the difference of the interpolate function $F_i(x)$. One of them is the first-order upwind method, which interpolates f_i^n by a linear function and satisfies following two constraints; $F_i(x_{i-1}) = f_{i-1}^n$ and $F_i(x_i) = f_i^n$ (here we assume that $u > 0$ and the upstream point for f_i^n locates left-side of x_i). The other variation is the Lax-Wendroff method, which uses a quadratic polynomial satisfying three constraints; $F_i(x_{i-1}) = f_{i-1}^n$, $F_i(x_i) = f_i^n$, and $F_i(x_{i+1}) = f_{i+1}^n$. We show these interpolation functions in Fig. 5.

On the contrary, the CIP method interpolates using a cubic polynomial, which satisfies following four constraints; $F_i(x_{i-1}) = f_{i-1}^n$, $F_i(x_i) = f_i^n$, $\partial F_i/\partial x(x_{i-1}) = f_{x,i-1}^n$, and $\partial F_i/\partial x(x_i) = f_{x,i}^n$, where $f_x \equiv \partial f/\partial x$ is the spatial gradient of f. The interpolation function is given by

$$F_i(x) = a_i(x - x_i)^3 + b_i(x - x_i)^2 + c_i(x - x_i) + d_i, \tag{12}$$

where a_i, b_i, c_i, and d_i are the coefficients determined from f_{i-1}^n, f_i^n, $f_{x,i-1}^n$, and $f_{x,i}^n$. The expressions of these coefficients are shown in (Yabe & Aoki, 1991). We show the profile of $F_i(x)$ in Fig. 5 with $f_{x,i-1}^n = f_{x,i}^n = 0$. In the CIP method, therefore, we need the values of f_x^n in addition of f^n for solving the advection phase.

In the CIP method, f_x is treated as an independent variable and updated independently from f as follows. Differentiating Eq. (10) with respect to x, we obtain

$$\frac{\partial f_x}{\partial t} + u\frac{\partial f_x}{\partial x} = -f_x\frac{\partial u}{\partial x}, \tag{13}$$

where the second term of the left-hand side indicates the advection term and the right-hand side indicates the non-advection term. The interpolate function for the advection of f_x is given by $\partial F_i/\partial x$. The non-advection term can be solved analytically by considering that $\partial u/\partial x$ is constant.

Additionally, there is an oscillation preventing method in the concept of the CIP method, in which the rational function is used as the interpolate function. The rational function is written as (Xiao et al., 1996)

$$F_i(x) = \frac{a_i(x-x_i)^3 + b_i(x-x_i)^2 + c_i(x-x_i) + d_i}{1 + \alpha_i\beta_i(x-x_i)}, \tag{14}$$

where α_i and β_i are coefficients. The expressions of these coefficients are shown in (Xiao et al., 1996). Usually, we adopt $\alpha_i = 1$ to prevent oscillation. This method is called as the R-CIP method. The model with $\alpha_i = 0$ corresponds to the normal CIP method.

3.1.2 CIP-CSL2 method

The CIP-CSL2 method is one of the numerical methods for solving the conservative equation. In one-dimension, the conservative equation is written as

$$\frac{\partial f}{\partial t} + \frac{\partial (uf)}{\partial x} = 0. \tag{15}$$

Integrating Eq. (15) over x from x_i to x_{i+1}, we obtain

$$\frac{\sigma_{i+1/2}}{\partial t} + [uf]_{x_i}^{x_{i+1}} = 0, \tag{16}$$

where $\sigma_{i+1/2} \equiv \int_{x_i}^{x_{i+1}} f dx$. For f being density, $\sigma_{i+1/2}$ corresponds to the mass contained in a computational cell between i and $i+1$, so it should be conserved during the time integration. Since the physical meaning of uf in the second term of the left-hand side is the flux of σ per unit area and per unit time, the time evolution of σ is determined by

$$\sigma_{i+1/2}^{n+1} = \sigma_{i+1/2}^{n} - J_{i+1} + J_i, \tag{17}$$

where $J_i \equiv \int_{t^n}^{t^{n+1}} uf dt$ is the transported value of σ from a region of $x < x_i$ to that of $x > x_i$ within Δt. The CIP-CSL2 method uses the integrated function $D_i(x) \equiv \int_{x_{i-1}}^{x} F_i(x)dx$ for the interpolation when $u_i > 0$. The function $D_i(x)$ is a cubic polynomial satisfying following four constraints; $D_i(x_{i-1}) = 0$, $D_i(x_i) = \sigma_{i-1/2}$, $\partial D_i/\partial x(x_{i-1}) = F_i(x_{i-1}) = f_{i-1}$, and $\partial D_i/\partial x(x_i) = F_i(x_i) = f_i$. Moreover, since Eq. (15) can be rewritten as the same form of Eq. (13), we can obtain the updated value f^{n+1} as well as f_x^{n+1} in the CIP method.

Additionally, there is an oscillation preventing method in the concept of the CIP-CSL2 method, in which the rational function is used for the function $D_i(x)$ (Nakamura et al., 2001). This method is called as the R-CIP-CSL2 method.

3.1.3 Anti-diffusion

To keep the sharp discontinuity in the profile of ϕ, we explicitly add an diffusion term with a negative diffusion coefficient α (anti-diffusion) to the CIP-CSL2 method (Miura & Nakamoto, 2007). In our model, we have an additional diffusion equation about σ as

$$\frac{\partial \sigma}{\partial t} = \frac{\partial}{\partial x}\left(\alpha \frac{\partial \sigma}{\partial x}\right). \tag{18}$$

Eq. (18) can be separated into two equations as

$$\frac{\partial \sigma}{\partial t} = -\frac{\partial J'}{\partial x}, \tag{19}$$

$$J' = -\alpha \frac{\partial \sigma}{\partial x}, \tag{20}$$

where J' indicates the anti-diffusion flux per unit area and per unit time. Using the finite difference method, we obtain

$$\sigma^{**}_{i+1/2} = \sigma^{*}_{i+1/2} - (\hat{J}'_{i+1} - \hat{J}'_{i}), \tag{21}$$

$$\hat{J}'_{i} = -\hat{\alpha}_i \times \mathrm{minmod}(S_{i-1}, S_i, S_{i+1}), \tag{22}$$

where $\hat{J} \equiv J'/(\Delta x/\Delta t)$ is the mass flux which has the same dimension of σ, $\hat{\alpha} \equiv \alpha/(\Delta x^2/\Delta t)$ is the dimensionless diffusion coefficient, and $S_i \equiv \sigma_{i+1/2} - \sigma_{i-1/2}$. The superscripts * and ** indicate the time step just before and after the anti-diffusion. The minimum modulus function (minmod) is often used in the concept of the flux limiter and has a non-zero value of $\mathrm{sign}(a)\min(|a|, |b|, |c|)$ only when a, b, and c have the same sign. The value of the diffusion coefficient $\hat{\alpha}$ is also important. Basically, we take $\hat{\alpha} = -0.1$ for the anti-diffusion. Here, it should be noted that σ takes the limited value as $0 \leq \sigma \leq \sigma_{\mathrm{m}}$, where σ_{m} is the initial value for inside of the droplet. The undershoot ($\sigma < 0$) or overshoot ($\sigma > \sigma_{\mathrm{m}}$) are physically incorrect solutions. To avoid that, we replace $\hat{\alpha}_i = 0.1$ only when $\sigma_{i-1/2}$ or $\sigma_{i+1/2}$ are out of the appropriate range. We insert the anti-diffusion calculation after the CIP-CSL2 method is completed.

3.1.4 Test calculation

In order to demonstrate the advantage of the CIP method, we carried out one-dimensional advection calculations with various numerical methods. Fig. 6 shows the spatial profiles of f of the test calculations. The horizontal axis is the spatial coordinate x. The initial profile is given by the solid line, which indicates a rectangle wave. We set the fluid velocity $u = 1$, the intervals of the grid points $\Delta x = 1$, and the time step for the calculation $\Delta t = 0.2$. These conditions give the CFL number $\nu \equiv u\Delta t/\Delta x = 0.2$, which indicates that the profile of f moves 0.2 times the grid interval per time step. Therefore, the right side of the rectangle wave will reach $x = 80$ after 300 time steps and the dashed line indicates the exact solution. The filled circles indicate the numerical results after 300 time steps.

The upwind method does not keep the rectangle shape after 300 time steps and the profile becomes smooth by the numerical diffusion (panel a). In the Lax-Wendroff method, the numerical oscillation appears behind the real wave (panel b). Comparing with above two methods, the CIP method seems to show better solution, however, some undershoots ($f < 0$)

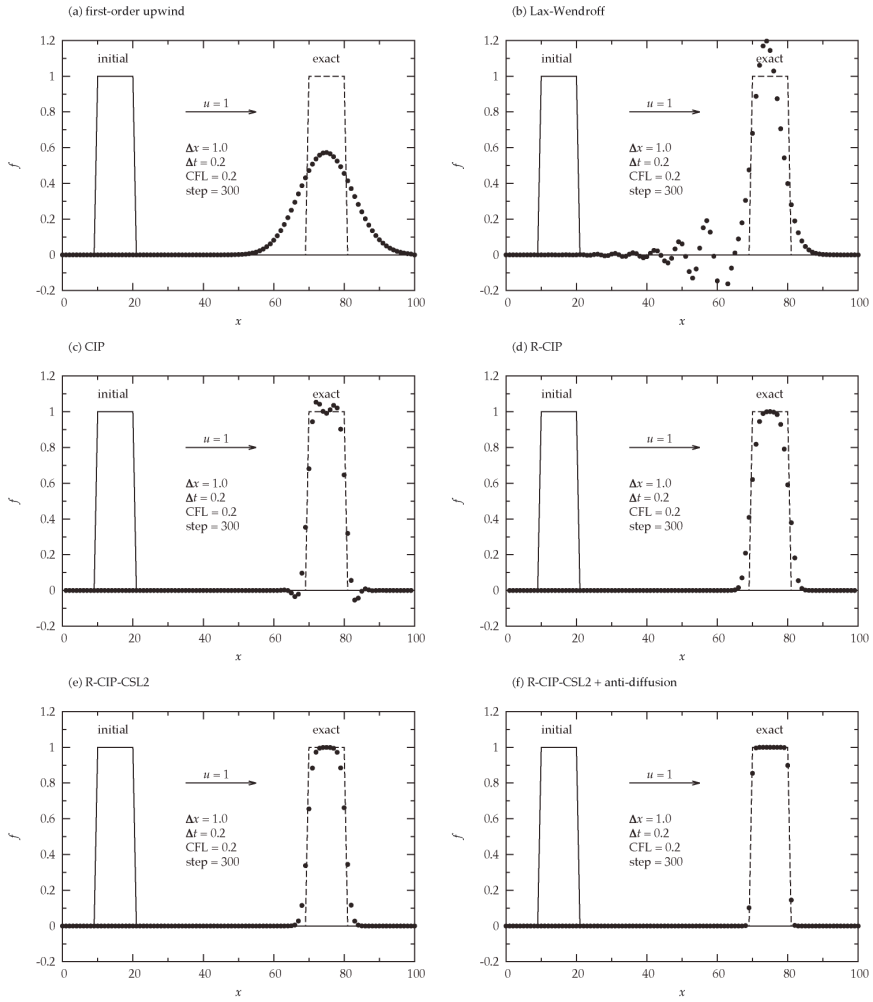

Fig. 6. Numerical solutions of the one-dimensional advection or conservation equation solved by various methods: (a) first-order upwind, (b) Lax-Wendroff, (c) CIP, (d) R-CIP, (e) R-CIP-CSL2 without anti-diffusion, and (f) R-CIP-CSL2 with anti-diffusion.

or overshoots ($f > 1$) are observed in the numerical result (panel c). In the R-CIP method, although the faint numerical diffusion has still remained, we obtain the excellent solution comparing with the above methods.

We also show the numerical results of the one-dimensional conservative equation. We use the same conditions with the one-dimensional advection equation. Note that Eq. (15) corresponds to Eq. (10) when the velocity u is constant. The panel (e) shows the result of the R-CIP-CSL2 method, which is similar to that of the R-CIP method. In the panel (f), we found that the combination of the R-CIP-CSL2 method and the anti-diffusion technique shows the excellent solution in which the numerical diffusion is prevented effectively.

3.2 Non-advection phase

3.2.1 C-CUP method

Using the finite difference method to Eq. (9), we obtain (Yabe & Wang, 1991)

$$\frac{\vec{u}^{**} - \vec{u}^{*}}{\Delta t} = -\frac{\vec{\nabla} p^{**}}{\rho^{*}} + \frac{\vec{Q}}{\rho^{*}}, \quad \frac{p^{**} - p^{*}}{\Delta t} = -\rho^{*} c_{\mathrm{s}}^{2} \vec{\nabla} \cdot \vec{u}^{**}, \tag{23}$$

where the superscripts * and ** indicate the times before and after calculating the non-advection phase, respectively. Since the sound speed is very large in the incompressible fluid, the term related to the pressure should be solved implicitly. In order to obtain the implicit equation for p^{**}, we take the divergence of the left equation and substitute $\vec{u}^{**}$ into the right equation. Then we obtain an equation

$$\vec{\nabla} \cdot \left(\frac{\vec{\nabla} p^{**}}{\rho^{*}} \right) = \frac{p^{**} - p^{*}}{\rho^{*} c_{\mathrm{s}}^{2} \Delta t^{2}} + \frac{\vec{\nabla} \cdot \vec{u^{*}}}{\Delta t} + \vec{\nabla} \cdot \left(\frac{\vec{Q}}{\rho^{*}} \right). \tag{24}$$

The problem to solve Eq. (24) resolves itself into to solve a set of linear algebraic equations in which the coefficients becomes an asymmetric sparse matrix. After p^{**} is solved, we can calculate $\vec{u}^{**}$ by solving the left equation in Eq. (23).

3.2.2 Ram pressure of free molecular flow

The ram pressure of the gas flow is acting on the droplet surface exposed to the high-velocity gas flow. It should be noted that the gas flow around a mm-sized droplet does not follow the hydrodynamical equations because the nebula gas is too rarefied. The mean free path of the nebula gas can be estimated by $l = 1/(ns)$, where s is the collisional cross section of gas molecules and n is the number density of the nebula gas. Typically, we adopt $n \approx 10^{14}$ cm^{-3} based on the standard model of the early solar system at a distance from the sun of an astronomical unit (Hayashi et al., 1985). Substituting $s \approx 10^{-16}$ cm^{-2} for the hydrogen molecule (Hollenbach & McKee, 1979), we obtain $l \approx 100$ cm. On the other hand, the typical size of chondrules is about a few 100 μm (see Fig. 3). Since the object that disturbs the gas flow is much smaller than the mean free path of the gas, the free stream velocity field is not disturbed except of the direct collision with the droplet (free molecular flow).

Consider that the molecular gas flows for the positive direction of the x-axis. The x-component of the ram pressure $F_{\mathrm{g},x}$ is given by

$$F_{\mathrm{g},x} = p_{\mathrm{fm}} \delta(x - x_{\mathrm{i}}), \tag{25}$$

where x_{i} is the position of the droplet surface. This equation can be separated into two equations as

$$F_{\mathrm{g},x} = -\frac{\partial M}{\partial x}, \quad \frac{\partial M}{\partial x} = -p_{\mathrm{fm}} \delta(x - x_{\mathrm{i}}), \tag{26}$$

where M is the momentum flux of the molecular gas flow. The right equation in Eq. (26) means that the momentum flux terminates at the droplet surface. The left equation in Eq. (26) means that the decrease of the momentum flux per unit length corresponding to the ram pressure per unit area.

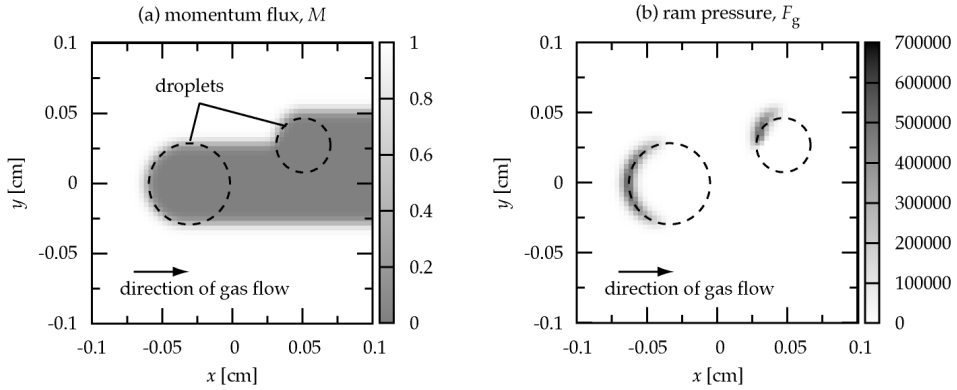

Fig. 7. Spatial distributions of the momentum flux M (a) and the ram pressure F_g (b) of the free molecular gas flow around a spherical droplet in xy-plane. The dashed circles are sections of the droplet surfaces in xy-plane. Units of the gray scales are p_{fm} for the panel (a) and dyn cm^{-3} for the panel (b), respectively. We adopt $p_{fm} = 5000$ dyn cm^{-2} in this figure.

Using the finite difference method to the right equation in Eq. (26), we obtain

$$M_{i+1} = M_i - p_{fm}(\bar{\phi}_{i+1} - \bar{\phi}_i) \quad \text{for } \bar{\phi}_{i+1} \geq \bar{\phi}_i, \tag{27}$$

where $\bar{\phi}$ is the smoothed profile of ϕ (see section 3.2.4), and $M_{i+1} = M_i$ for $\bar{\phi}_{i+1} < \bar{\phi}_i$ because the momentum flux does not increase when the molecular flow goes outward from inside of the droplet. Similarly, we obtain

$$F_{g,x_i} = -\frac{M_i - M_{i+1}}{\Delta x}, \tag{28}$$

from the left equation in Eq. (26). The momentum flux at upstream is $M_0 = p_{fm}$. First, we solve Eq. (27) and obtain the spatial distribution of the molecular gas flow in all computational domain. Then, we calculate the ram pressure by Eq. (28).

Fig. 7(a) shows the distribution of momentum flux M around two droplets in xy-plane. The dashed circles are the external shapes of large and small droplets. The gray scale is normalized by p_{fm}, so unity (white region) means undisturbed molecular flow and zero (dark region) means no flux because the free molecular flow is obstructed by the droplet. It is found that the gas flow is obstructed only behind the droplets. Fig. 7(b) shows the distribution of the ram pressure $F_{g,x}$ calculated from the momentum flux distribution. The ram pressure is acting at the droplet surface where M changes steeply. Note that no ram pressure acts at bottom half of the smaller droplet because the molecular flow is obstructed by the larger one. As shown in Fig. 7, the model of ram pressure shown here well reproduces the property of free molecular flow.

We calculate the momentum flux M and the ram pressure F_g at every time step in numerical simulations. Therefore, these spatial distributions are affected by droplet deformation.

3.2.3 Surface tension

The surface tension is the normal force per unit interfacial area. Brackbill et al. (Brackbill et al., 1992) introduced a method to treat the surface tension as a volume force by replacing the

discontinuous interface to the transition region which has some width. According to them, the surface tension is expressed as

$$\vec{F}_s = \gamma_s \kappa \vec{\nabla}\phi / [\phi], \tag{29}$$

where $[\phi]$ is the jump in color function at the interface between the droplet and the ambient gas. In our definition, we obtain $[\phi] = 1$. The curvature is given by

$$\kappa = -(\vec{\nabla} \cdot \vec{n}), \tag{30}$$

where

$$\vec{n} = \vec{\nabla}\phi / |\vec{\nabla}\phi|. \tag{31}$$

The finite difference method of Eq. (31) is shown in (Brackbill et al., 1992). When we calculate the surface tension, we use the smoothed profile of ϕ (see section 3.2.4).

3.2.4 Smoothing

We can obtain the numerical results keeping the sharp interface between the droplet and the ambient region. However, the smooth interface is suitable for calculating the smooth surface tension. We use the smoothed profile of ϕ only at the time to calculate the surface tension and the ram pressure acting on the droplet surface. In this study, the smoothed color function $\bar{\phi}$ is calculated by

$$\bar{\phi} = \frac{1}{2}\phi_{i,j,k} + \frac{1}{2}\frac{\phi_{i,j,k} + C_1 \sum_{L_1}^{6} \phi_{L_1} + C_2 \sum_{L_2}^{12} \phi_{L_2} + C_3 \sum_{L_3}^{8} \phi_{L_3}}{1 + 6C_1 + 12C_2 + 8C_3}, \tag{32}$$

where L_1, L_2, and L_3 indicate grid indexes of the nearest, second nearest, and third nearest from the grid point (i, j, k), for example, $L_1 = (i+1, j, k)$, $L_2 = (i+1, j+1, k)$, $L_3 = (i+1, j+1, k+1)$, and so forth. It is easily found that in the three-dimensional Cartesian coordinate system, there are six for L_1, twelve for L_2, and eight for L_3, respectively. The coefficients are set as

$$C_1 = 1/(6 + 12/\sqrt{2} + 8/\sqrt{3}), \quad C_2 = C_1/\sqrt{2}, \quad C_3 = C_1/\sqrt{3}. \tag{33}$$

We iterate the smoothing five times. Then, we obtain the smooth transition region of about twice grid interval width. We use the smooth profile of ϕ only when calculating the surface tension and the ram pressure. It should be noted that the original profile ϕ with the sharp interface is kept unchanged.

4. Deformation of droplet by gas flow

4.1 Vibrational motion

We assume that the gas flow suddenly affects the initially spherical droplet. Fig. 8 shows the time sequence of the droplet shape and the internal velocity. The horizontal and vertical axes are the x- and y-axes, respectively. The solid line is the section of the droplet surface in xy-plane. Arrows show the velocity field inside the droplet. The gas flow comes from the left side of the panel. The panel (a) shows the initial condition for the calculation. The panel (b) shows a snapshot at $t = 0.55$ msec. The droplet begins to be deformed due to the gas ram pressure. The fluid elements at the surface layer, which is directly facing the gas flow, are blown to the downstream. In contrast, the velocity at the center of the droplet turns to

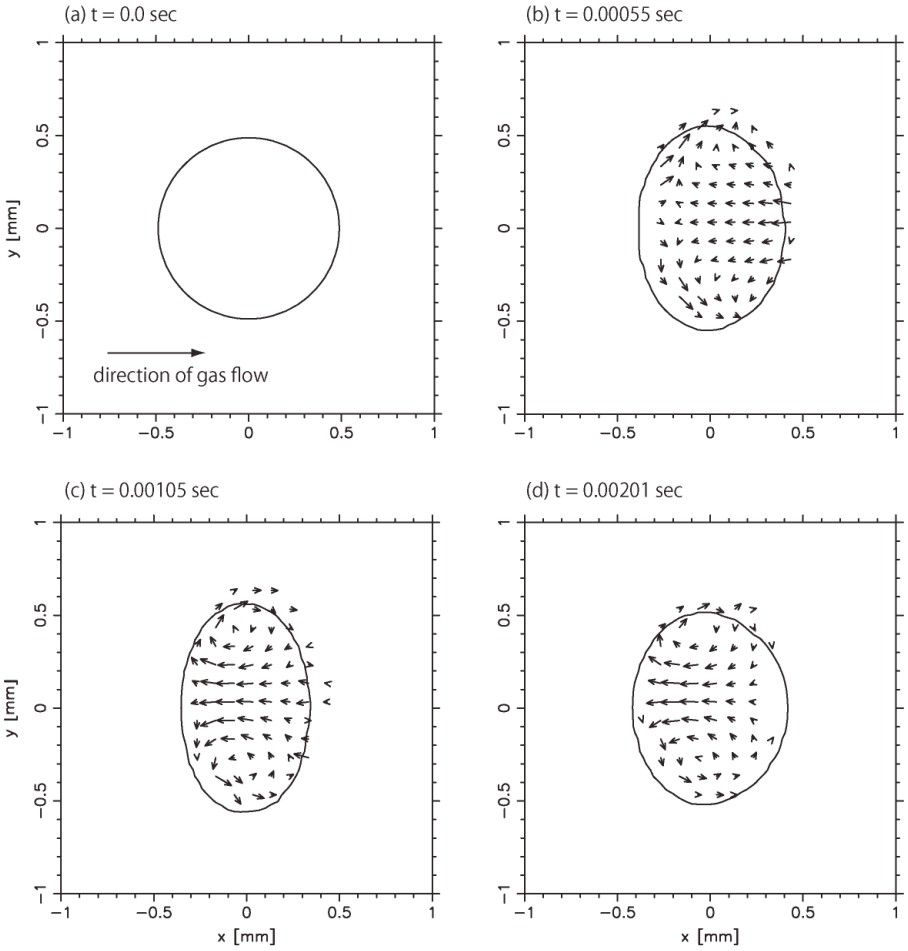

Fig. 8. Time evolution of molten droplet exposed to the gas flow. The gas flow comes from the left side of panels. We use $p_{\mathrm{fm}} = 10^4$ dyn cm^{-2}, $r_0 = 500$ ¯m, and $\mu_{\mathrm{d}} = 1.3$ poise for calculations.

upstream of the gas flow because the apparent gravitational acceleration takes place in our coordinate system. The droplet continues to be deformed further, and after $t = 1.0$ msec, the degree of deformation becomes maximum (see panel (c)). After that, the droplet begins to recover its shape to the sphere due to the surface tension. The recovery motion is not all but almost over at the panel (d). The droplet repeats the deformation by the ram pressure and the recovery motion by the surface tension until the viscosity dissipates the internal motion of the droplet.

Fig. 9 shows the time variation of axial ratio c/b of the droplet. Each curve shows the calculation result for the different value of the ram pressure p_{fm}. The droplet is compressed unidirectionally by the gas flow, so the length of minor axis c corresponds to the half length of droplet axis in the direction of the gas flow. The axial ratio c/b is unity at the

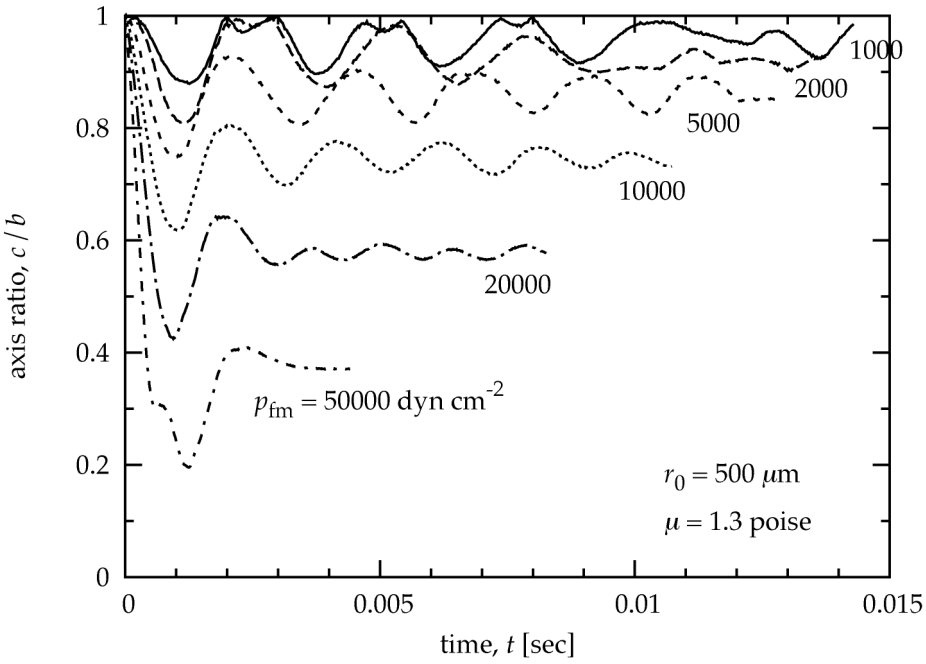

Fig. 9. Vibrational motions of molten droplet; the deformation by the ram pressure and the recovery motion by the surface tension. The horizontal axis is the time since the ram pressure begins to affect the droplet and the vertical axis is the axial ratio of the droplet c/b. Each curve shows the calculation result for the different value of the ram pressure p_{fm}. We use $r_0 = 500$ ¯m and $\mu_d = 1.3$ poise for calculations.

beginning because the initial droplet shape is a perfect sphere. The axial ratio decreases as time goes by because of the compression. After about 1 msec, c/b reaches minimum and then increases due to the surface tension. After this, the axial ratio vibrates with a constant frequency and finally the vibrational motion damps due to viscous dissipation. The calculated frequency of the vibrational motion is about 2 msec not depending on p_{fm}. The calculated frequency is consistent with that of a capillary oscillations of a spherical droplet given by $P_{vib} = 2\pi\sqrt{\rho_d r_0^3/8\gamma_s} \approx 2.15$ msec (Landau & Lifshitz, 1987).

4.2 Overdamping

Fig. 10 shows the time variation of the axial ratio c/b when the viscosity is 100 times larger than that in Fig. 9. It is found that the axial ratio converges on the value at steady state without any vibrational motion. This is an overdamping due to the strong viscous dissipation.

4.3 Effect of droplet rotation

We carried out the hydrodynamics simulations of non-rotating molten droplet in previous sections. However, the rotation of the droplet should be taken into consideration as the following reason. A chondrule before melting is an aggregate of numerous fine particles,

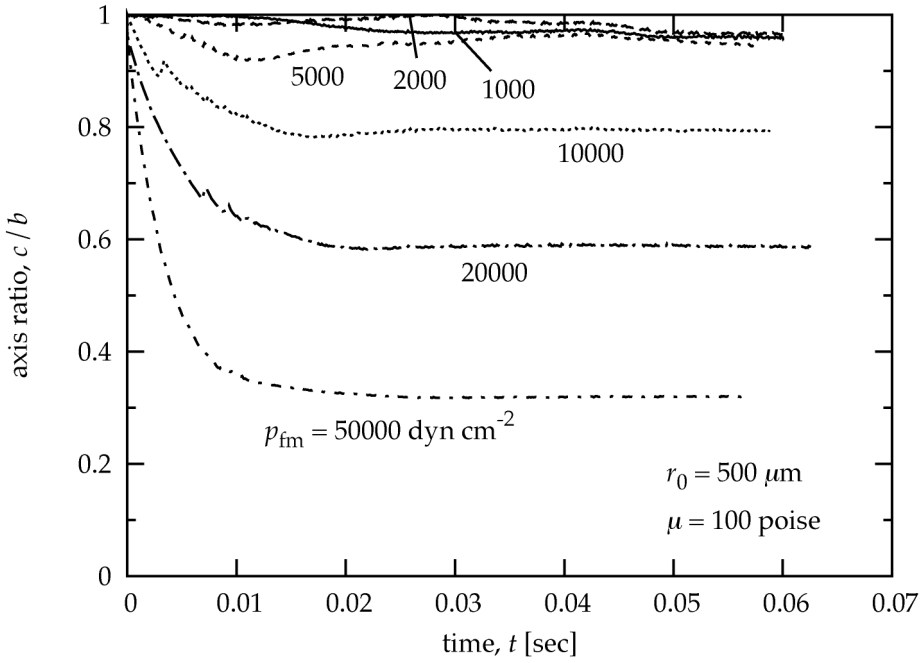

Fig. 10. Same as Fig. 9 except of $\mu_{\rm d} = 100$ poise.

so the shape is irregular in general. The irregular shape causes a net torque in an uniform gas flow. Therefore, it is naturally expected that the molten chondrule also rotates at a certain angular velocity.

The angular velocity ω_f can be roughly estimated by $I\omega_f \approx N\Delta t$, where I is the moment of inertia of chondrule and Δt is the duration to receive the net torque N. Assuming that the small fraction f of the cross-section of the precursor contributes to produce the net torque N, we obtain $N \approx f\pi r_0^3 p_{\rm fm}$. We can set $\Delta t \approx \pi/\omega_f$ (a half-rotation period) because the sign of N would change after half-rotation. Substituting $I = (8/15)\pi r_0^5 \rho_{\rm d}$, which is the moment of inertia for a sphere with an uniform density $\rho_{\rm d}$, we obtain the angular velocity (Miura, Nakamoto & Doi, 2008)

$$\begin{aligned}\omega_f &\approx \sqrt{15 f \pi p_{\rm fm}/8 r_0^2 \rho_{\rm d}} \\ &= 140 \left(\frac{f}{0.01}\right)^{1/2} \left(\frac{p_{\rm fm}}{10^4 \text{ dyn cm}^{-2}}\right)^{1/2} \left(\frac{r_0}{1 \text{ mm}}\right)^{-1} \text{ rad s}^{-1}. \end{aligned} \tag{34}$$

Therefore, in the shock-wave heating model, the droplet should be rotating rapidly if most of the angular momentum is maintained during melting.

In addition, it should be noted that the rotation axis is likely to be perpendicular to the direction of the gas flow unless the chondrule before melting has a peculiar shape as windmill.

Fig. 11 shows the deformation of a rotating droplet in gas flow in a three-dimensional view. The rotation axis is set to be perpendicular to the direction of the gas flow. We use $\mu_{\rm d} =$

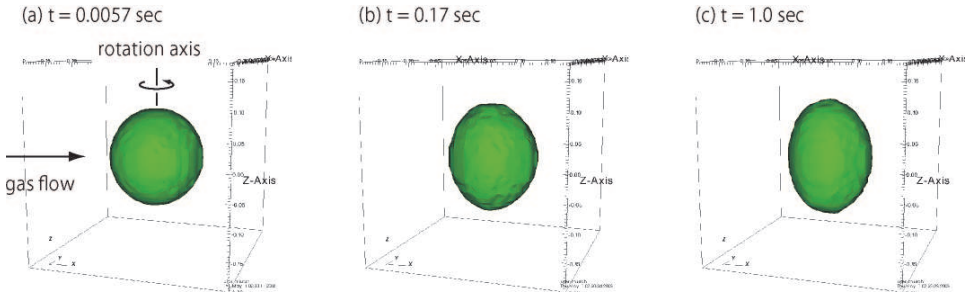

Fig. 11. Three-dimensional view of a rotating molten droplet exposed to a high-velocity gas flow. The object shows the external shape of the droplet (iso-surface of the color function of $\phi = 0.5$). The gas flow comes from the left side (arrow). The rotation axis of the droplet is perpendicular to the direction of the gas flow. After $t = 1.0$ sec, the droplet shape becomes a prolate. We use $\mu_{\rm d} = 10^3$ poise, $p_{\rm fm} = 10^4$ dyn cm^{-2}, $\omega = 100$ rad s^{-1}, and $r_0 = 1$ mm.

10^3 poise, $p_{\rm fm} = 10^4$ dyn cm^{-2}, $\omega = 100$ rad s^{-1}, and $r_0 = 1$ mm. It is found that the droplet elongates in a direction of the rotation axis as the time goes by. Fig. 12 shows the time variation of the axial ratios b/a (solid) and c/b (dashed). The major axis a corresponds to the droplet radius in a direction of the gas flow, so the decrease of b/a means the droplet elongation. The axial ratio b/a reaches a steady value of 0.76 after 1 sec. The axial ratio c/b is kept at a constant value of ≈ 0.95 during the calculation, which means that two droplet radius perpendicular to the rotation axis is almost uniform. The droplet shape at the steady state is prolate, in other words, a rugby-ball-like shape.

4.4 Origin of prolate chondrule

Why did the droplet shape become prolate? The reason, of course, is due to the droplet rotation. If there is no rotation on the droplet, its shape is only affected by the gas which comes from the fixed direction (see Fig. 13a). In this case, the droplet shape becomes disk-like (oblate) shape because only one axis, which corresponds to the direction of the gas flow, becomes shorter than the other two axes (Sekiya et al., 2003). In contrast, let us consider the case that the droplet is rotating. If the rotation period is much shorter than the viscous deformation timescale, the gas flow averaged during one rotation period can be considered to be axis-symmetrical about the rotation axis (see Fig. 13b). Therefore, the droplet shrinks due to the axis-symmetrical gas flow along directions perpendicular to the rotation axis and becomes prolate if the averaged gas ram pressure is strong enough to overcome the centrifugal force.

Doi (Doi, 2011) derived the analytic solution of deformation of a rotating droplet in gas flow in a case that the gas flow can be approximated as axis-symmetrical around the rotation axis as shown in Fig. 13(b). He considered that the droplet radius is given by $r(\theta) = r_0 + r_1(\theta)$, where r_0 is the unperturbed droplet radius and r_1 is the deviation from a perfect sphere. θ is the angle between the position (the origin is the center of the droplet) and the rotation axis. According to his solution, the droplet deformation is given by

$$\frac{r_1(\theta)}{r_0} = \frac{W_e}{12}\left(\frac{19}{20} - R\right) P_2(\cos\theta), \tag{35}$$

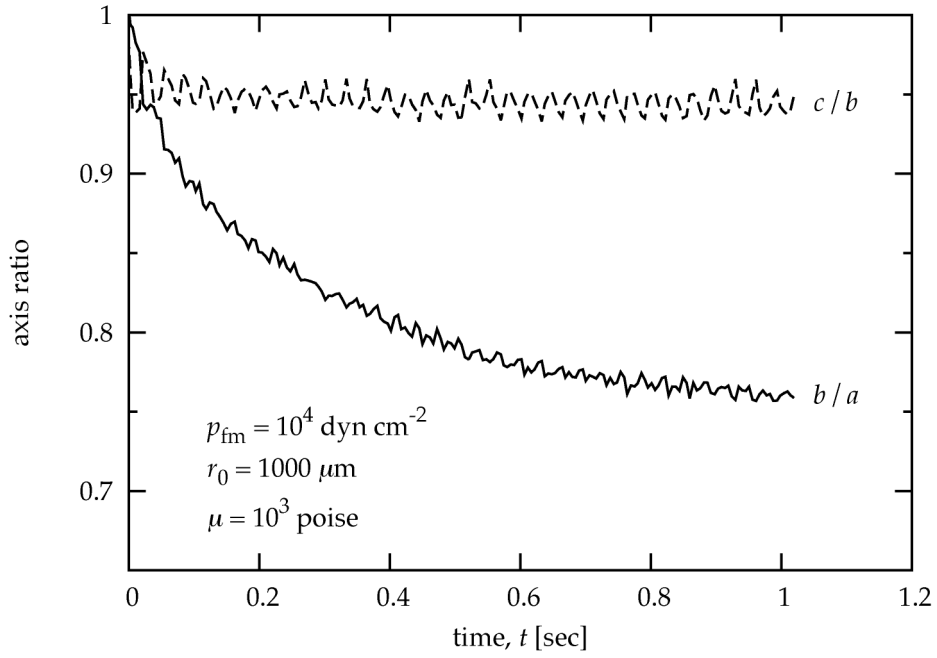

Fig. 12. Time evolutions of axial ratios b/a and c/b in the case of Fig. 11.

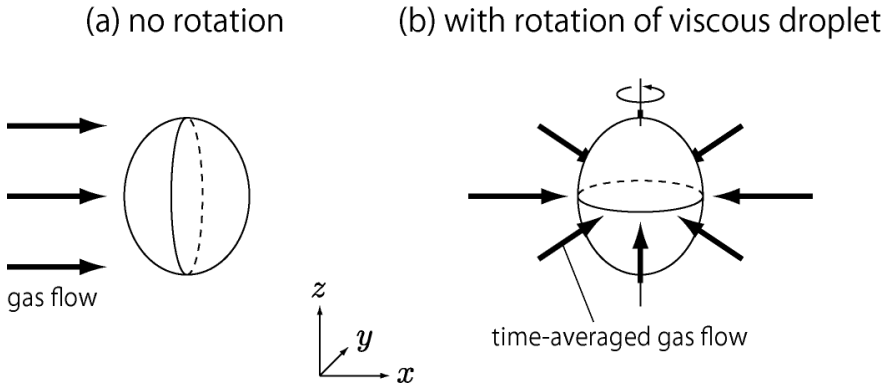

Fig. 13. The reason why the rotating droplet exposed to the gas flow is deformed to a prolate shape is illustrated. (a) If the droplet does not rotate, it is deformed only by the effect of the gas ram pressure. (b) If the droplet rotates much faster than the deformation due to the gas flow, the time-averaged gas flow can be approximated as axis-symmetrical around the rotation axis.

where W_e (Weber number) is the ratio of the ram pressure of the gas flow to the surface tension of the droplet defined as

$$W_e = \frac{p_{\rm fm} r_0}{\gamma_{\rm s}}, \tag{36}$$

R is the ratio of the centrifugal force to the ram pressure defined as

$$R = \frac{\rho_{\rm d} r_0^2 \omega^2}{p_{\rm fm}}, \tag{37}$$

ω is the angular velocity of the rotation, and $P_l(\cos\theta)$ is Legendre polynomials. This solution is applicable under the assumption of $r_1 \ll r_0$. Eq. (35) shows that the particle radius becomes the maximum at $\theta = 0$, and minimum at $\theta = \pi/2$. $R = 19/20$ is a critical value for the droplet shape to be prolate ($R < 19/20$) or oblate ($R > 19/20$). The droplet shape is sphere when $R = 19/20$ because the ram pressure balances with the centrifugal force.

Fig. 14 shows the droplet shape as functions of the Weber number W_e and the normalized centrifugal force R using Eq. (35). $R = 19/20$ (vertical dashed line) is a critical value for the droplet shape to be prolate ($R < 19/20$) or oblate ($R > 19/20$). In the prolate region, the axial ratio b/a is less than unity for $W_e > 0$ as shown by contours, but $c/b = 1$. On the other hand, in the oblate region, the axial ratio c/b is less than unity for $W_e > 0$, but $b/a = 1$. As W_e increases, the degree of deformation increases as shown in decrease of axial ratio b/a or c/b. The blue and red regions show ranges of axial ratios of group-A spherical chondrules and group-B prolate chondrules, respectively. We carried out the hydrodynamics simulations for a wide range of parameters and displayed on this diagram by symbols. It is found that the hydrodynamics simulation results show a good agreement with the analytic solution for a wide range of W_e and R.

Let us consider the shape of chondrule expected from the shock-wave heating model. Adopting ram pressure of the gas flow of $p_{\rm fm} = 10^4$ dyn cm^{-2} and the radius of chondrule of $r_0 = 1$ mm, we obtain $W_e = 2.5$ for $\gamma_{\rm s} = 400$ erg cm^{-2}. According to Eq. (34), we evaluate $R = 0.06$ for $f = 0.01$. The evaluated value of R is smaller than the critical value of 19/20, so the expected droplet shape is prolate. In addition, the axial ratio b/a comes into a range of group-B prolate chondrules (see Fig. 14). This suggests that the origin of group-B prolate chondrules can be explained by the shock-wave heating model. Of course, it should be noted that the shock-wave heating model does not reproduce the group-B prolate chondrules for arbitrary conditions because W_e and R depend on many factors, e.g., $p_{\rm fm}$, r_0, and f. Namely, it is possible that different shock conditions produce different chondrule shapes, even out of the range of group-A or -B. This fact, on the contrary, indicates that the chondrule shapes constrain shock conditions suitable for formation of these chondrules. The data of three-dimensional chondrule shapes measured by Tsuchiyama et al. (Tsuchiyama et al., 2003) is definitely valuable, however, the number of samples is twenty at most. We need more data to constrain the chondrule formation mechanism from their three-dimensional shapes.

5. Fragmentation

5.1 Direct fragmentation

When the droplet size is too large for the surface tension to keep the droplet shape against the gas ram pressure, the fragmentation will occur. Fig. 15 shows the three-dimensional views of

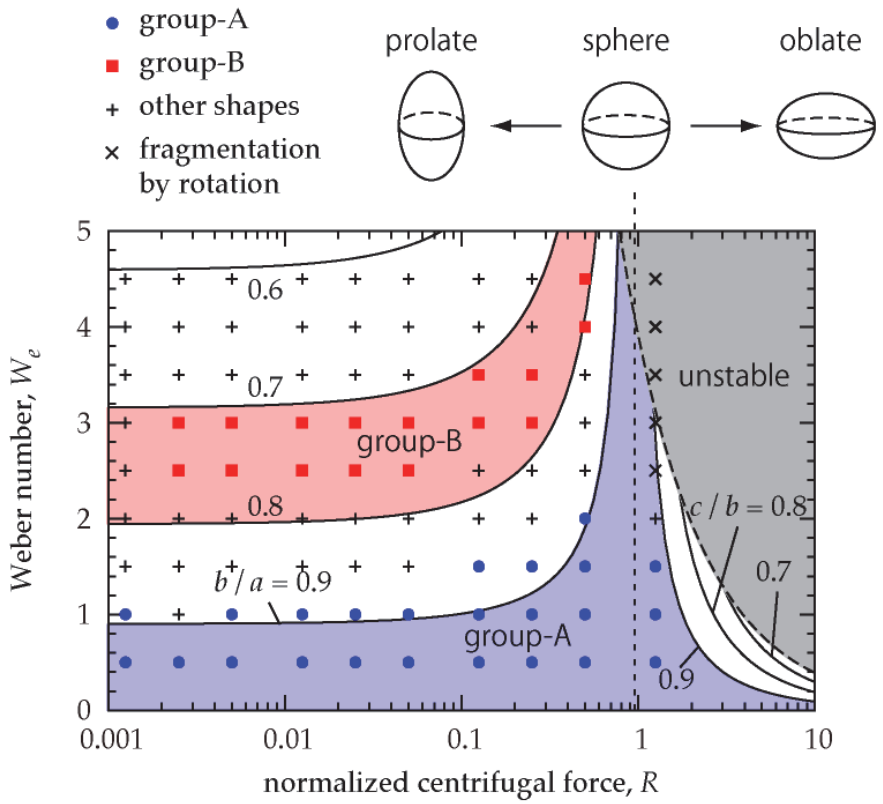

Fig. 14. Shapes of rotating droplets in gas flow. The horizontal axis is the centrifugal force normalized by ram pressure of the gas flow R. The vertical axis is the Weber number W_e. $R = 19/20$ (vertical dashed line) is a critical value for the droplet shape to be prolate ($R < 19/20$) or oblate ($R > 19/20$). Solid lines are contours of axial ratios of b/a ($R < 19/20$) or c/b ($R > 19/20$). A ranges of axial ratios of chondrules are shown by colored regions for group-A spherical chondrules (blue) and for group-B prolate chondrules (red), respectively. Symbols are results of hydrodynamics simulations (see legends in figure). Grayed region shows a condition in which the droplet will be fragmented by rapid rotation.

the break-up droplet. The droplet radius is $r_0 = 2$ cm, which corresponds to $W_e = 20$. The gas flow comes from the left side of the view along the x-axis. It is found that the droplet shape is deformed as the time goes by (panels (a) and (b)), and leads to fragmentation (panel (c)). The parent droplet breaks up to many smaller pieces.

Susa & Nakamoto (Susa & Nakamoto, 2002) suggested that the fragmentation of the droplets in high-velocity gas flow limits the sizes of chondrules (upper limit). They considered the balance between the surface tension and the inhomogeneity of the ram pressure acting on the droplet surface, and derived the maximum size of molten silicate dust particles above which the droplet would be destroyed by the ram pressure of the gas flow using an order of magnitude estimation. In their estimation, they adopted the experimental data in which

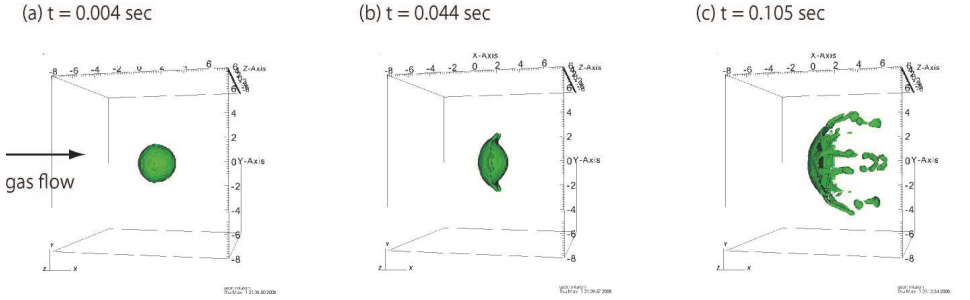

Fig. 15. Three-dimensional view of the fragmentation of molten droplet. We use $\mu_{\rm d} = 1$ poise, $p_{\rm fm} = 4000$ dyn cm^{-2}, and $r_0 = 2$ cm. The calculation was performed on a $100 \times 100 \times 100$ grid.

the droplets suddenly exposed to the gas flow fragment for $W_e >\sim 6$ (Bronshten, 1983, p.96). This results into the fragmentation of droplet for $r_0 >\sim 6$ mm if we adopt our calculation conditions: $p_{\rm fm} = 4000$ dyn cm^{-2} and $\gamma_{\rm s} = 400$ dyn cm^{-1}. Our hydrodynamics simulations agree with the criterion for fragmentation.

5.2 Fragmentation via cavitation

Fig. 16 shows the internal pressure inside the droplet for various droplet sizes: $r_0 = 3$, 4, and 5 mm from panels (a) to (c). We use $\mu_{\rm d} = 1.3$ poise and $p_{\rm fm} = 4000$ dyn cm^{-2}. These droplets reach steady states, so their hydrodynamics do not change significantly after these panels. We found a high pressure region at the front of the droplet, and low pressure regions at centers of eddies in all cases. The high pressure is due to the ram pressure of the gas flow. The low pressure in eddy is clearly due to the non-linear effect caused by the advection term in Eq. (2). Surprisingly, the pressure in eddy decreases to almost zero in panels (b) and (c). In the "zero"-pressure region, the vaporization (or boiling) of the liquid would take place because the vapor pressure of the liquid exceeds the internal pressure. This phenomenon is well known as cavitation. We did not take into account the cavitation in our simulations, so no vaporization occurred in the calculation. If the cavitation was taken into consideration, the eddies are no longer maintained because of the cavitation, which would cause the fragmentation of the droplet.

Miura & Nakamoto (Miura & Nakamoto, 2007) proposed the condition for the "zero"-pressure region to appear by considering the balance between the centrifugal force and the pressure gradient force around eddies as $\rho_{\rm d} v_{\rm circ}^2 / r_{\rm eddy} \approx p / r_{\rm eddy}$, where $v_{\rm circ}$ is the fluid velocity around the eddy, $r_{\rm eddy}$ is the radius of the eddy, and p is the pressure inside the droplet. Substituting $p = 2\gamma_{\rm s}/r_0$ from the Young-Laplace equation and $v_{\rm circ} \approx v_{\rm max} = 0.112 p_{\rm fm} r_0 / \mu_{\rm d}$ (Sekiya et al., 2003), we obtain

$$r_{0,\rm cav} \approx \left(\frac{2\gamma_{\rm s}\mu_{\rm d}^2}{0.112^2 \rho_{\rm d} p_{\rm fm}^2} \right)^{1/3} . \tag{38}$$

This equation gives the critical radius of the droplet above which the cavitation takes place in the center of the eddy. We obtain $r_{0,\rm cav} = 1.3$ mm for the calculation condition. In our hydrodynamic simulations, we observed the "zero"-pressure region for $r_0 = 4$ mm or larger.

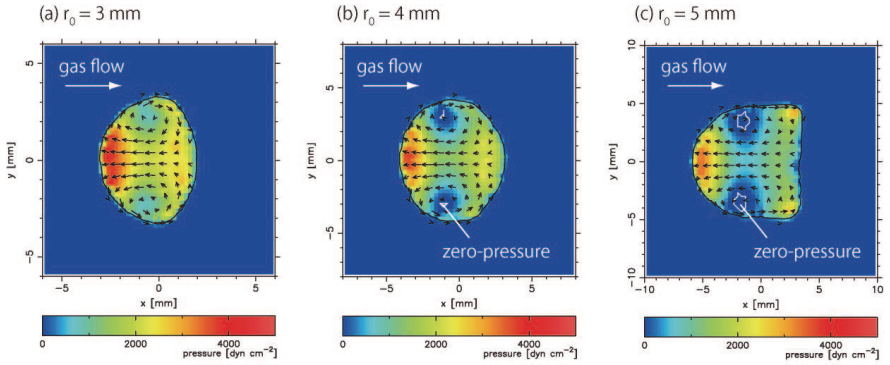

Fig. 16. Internal pressure inside droplet for different droplet radius r_0: (a) 3 mm, (b) 4 mm, and (c) 5 mm. The pressure at a region surrounded by a white line decreases to almost zero by the eddy. We use $\mu_{\rm d} = 1.3$ poise and $p_{\rm fm} = 4000$ dyn cm^{-2}.

The inconsistency of cavitation criterion between hydrodynamics simulation and Eq. (38) might come from the fact that we substitute the linear solution into $v_{\rm circ}$. The Sekiya's solution did not take into account the non-linear term in the Navier-Stokes equation. On the other hand, the cavitation would be caused by the non-linear effect. The substitution of the linear solution into the non-linear phenomenon might be a reason for the inconsistency. However, Eq. (38) provide us an insight of the cavitation criterion qualitatively.

5.3 Comparison with chondrule properties

It was found from the chondrule size distribution (see Fig. 3) that chondrules larger than a few mm in radius are very rare. The origin of the chondrule size distribution has been considered as some size-sorting process prior to chondrule formation in the early solar gas disk (Teitler et al., 2010, and references therein). On the other hand, in the framework of the shock-wave heating model, the upper limit of chondrule sizes can be explained by the fragmentation of a molten chondrule in high-velocity gas flow. The criterion of fragmentation is given by $W_e = p_{\rm fm} r_0 / \gamma_{\rm s} \approx 6$. Since the ram pressure of the gas flow is typically $p_{\rm fm} \approx 10^3 - 10^5$ dyncm^{-2}, we obtain the upper limit of chondrule sizes as $r_{\rm max} \approx 0.2 - 20$ mm. This is consistent with the fact that chondrules larger than a few mm in radius are very rare.

In addition, our hydrodynamics simulations show a new pathway to the fragmentation by cavitation. The cavitation takes place for $W_e < 6$ if viscosity of the molten chondrule is small. The viscosity decreases rapidly as temperature of the droplet increases. This suggests the following tendency: chondrules that experienced higher maximum temperature during melting have smaller sizes that that experienced lower maximum temperature. On the other hand, the data obtained by Nelson & Rubin (Nelson & Rubin, 2002) showed the tendency opposite from our prediction. They considered the reason of the difference in mean sizes among chondrule textural types being due mainly to parent-body chondrule-fragmentation events and not to chondrule-formation processes in the solar nebula. Therefore, to date, there is no evidence regarding the dependence of chondrule sizes on the maximum temperature. The relation between the chondrule sizes and the maximum temperature should be investigated in the future.

How about the distribution of sizes smaller than the maximum one? Kadono and his colleagues carried out aerodynamic liquid dispersion experiments using shock tube (Kadono & Arakawa, 2005; Kadono et al., 2008). They showed that the size distributions of dispersed droplets are represented by an exponential form and similar form to that of chondrules. In their experimental setup, the gas pressure is too high to approximate the gas flow around the droplet as free molecular flow. We carried out the hydrodynamics simulations of droplet dispersion and showed that the size distribution of dispersed droplets is similar to the Kadono's experiments (Yasuda et al., 2009). These results suggest that the shock-wave heating model accounts for not only the maximum size of chondrules but also their size distribution below the maximum size.

In addition, we recognized a new interesting phenomenon relating to the chondrule formation: the droplets dispersed from the parent droplet collide each other. A set of droplets after collision will fuse together into one droplet if the viscosities are low. In contrary, if the set of droplets solidifies before complete fusion, it will have a strange morphology that is composed of two or more chondrules adhered together. This is known as compound chondrules and has been observed in chondritic meteorites in actuality. The abundance of compound chondrules relative to single chondrules is about a few percents at most (Akaki & Nakamura, 2005; Gooding & Keil, 1981; Wasson et al., 1995). The abundance sounds rare, however, this is much higher comparing with the collision probability of chondrules in the early solar gas disk, where number density of chondrules is quite low (Gooding & Keil, 1981; Sekiya & Nakamura, 1996). In the case of collisions among dispersed droplets, a high collision probability is expected because the local number density is high enough behind the parent droplet (Miura, Yasuda & Nakamoto, 2008; Yasuda et al., 2009). The fragmentation of a droplet in the shock-wave heating model might account for the origin of compound chondrules.

6. Conclusion

To conclude, hydrodynamics behaviors of a droplet in space environment are key processes to understand the formation of primitive materials in meteorites. We modeled its three-dimensional hydrodynamics in a hypervelocity gas flow. Our numerical code based on the CIP method properly simulated the deformation, internal flow, and fragmentation of the droplet. We found that these hydrodynamics results accounted for many physical properties of chondrules.

7. References

Akaki, T. & Nakamura, T. (2005). Formation processes of compound chondrules in cv3 carbonaceous chondrites: Constraints from oxygen isotope ratios and major element concentrations., *Geochim. Cosmochim. Acta* 69: 2907–2929.

Amelin, T., Krot, A. N., Hutcheon, I. D. & Ulyanov, A. A. (2002). Lead isotopic ages of chondrules and calcium-aluminum-rich inclusions, *Science* 297: 1678–1683.

Amelin, Y. & Krot, A. (2007). Pb isotopic age of the allende chondrules, *Meteorit. Planet. Sci.* 42: 1321–1335.

Blander, M., Planner, H., Keil, K., Nelson, L. & Richardson, N. (1976). The origin of chondrules: experimental investigation of metastable liquids in the system mg2sio4-sio2, *Geochimica et Cosmochimica Acta* 40(8): 889 – 892, IN1–IN2, 893–896.

URL: *http://www.sciencedirect.com/science/article/B6V66-48C8H7W-BK/2/bdd79a0a3820afc4d06ac02bdc7cfaa7*

Brackbill, J. U., Kothe, D. B. & Zemach, C. (1992). A continuum method for modeling surface tension, *Journal of Computational Physics* 100(2): 335 – 354.
URL: *http://www.sciencedirect.com/science/article/pii/002199919290240Y*

Bronshten, V. A. (1983). *Physics of Meteoric Phenomena*, Dordrecht: Reidel.

Chandrasekhar, S. (1965). The stability of a rotating liquid drop, *Proceedings of the Royal Society of London. Ser. A, Mathematical and Physical Sciences* 286: 1–26.

Ciesla, F. J. & Hood, L. L. (2002). The nebula shock wave model for chondrule formation: Shock processing in a particle-gas suspension, *Icarus* 158: 281–293.

Ciesla, F. J., Hood, L. L. & Weidenschilling, S. J. (2004). Evaluating planetesimal bow shocks as sites for chondrule formation, *Meteorit. Planet. Sci.* 39: 1809–1821.

Desch, S. J. & Jr., H. C. C. (2002). A model of the thermal processing of particles in solar nebula shocks: Application to the cooling rates of chondrules, *Meteorit. Planet. Sci.* 37: 183–207.

Doi, M. (2011). *Formation of cosmic spherule: chemical analysis and theory for shapes, compositions, and textures*, PhD thesis, Tokyo Institute of Technology.

Fredriksson, K. & Ringwood, A. (1963). Origin of meteoritic chondrules, *Geochimica et Cosmochimica Acta* 27(6): 639 – 641.
URL: *http://www.sciencedirect.com/science/article/B6V66-48C8FST-5/2/baf33fee9f7f0a8d0a3ef0a92ac38cf7*

Gooding, J. L. & Keil, K. (1981). Relative abundances of chondrule primary textural types in ordinary chondrites and their bearing on conditions of chondrule formation, *Meteoritics* 16: 17–43.

Harold C. Connolly, J. & Hewins, R. H. (1995). Chondrules as products of dust collisions with totally molten droplets within a dust-rich nebular environment: An experimental investigation, *Geochimica et Cosmochimica Acta* 59: 3231–3246.

Hayashi, C. K., Nakazawa, K. & Nakagawa, Y. (1985). *Formation of the solar system*, Protostars and Planets II, Univ. of Arizona Press, Tucson, pp. 1100–1153.

Hewins, R. H. & Radomsky, P. M. (1990). Temperature conditions for chondrule formation, *Meteoritics* 25: 309–318.

Hollenbach, D. & McKee, C. F. (1979). Molecular formation and infrared emission in fast interstellar shocks. i. physical proceses, *Astrophys. J.* 41: 555–592.

Hood, L. L. (1998). Thermal processing of chondrule precursors in planetesimal bow shocks, *Meteorit. Planet. Sci.* 33: 97–108.

Hood, L. L. & Horanyi, M. (1991). Gas dynamic heating of chondrule precursor grains in the solar nebula, *Icarus* 93: 259–269.

Hood, L. L. & Horanyi, M. (1993). The nebular shock wave model for chondrule formation - one-dimensional calculations, *Icarus* 106: 179–189.

Hughes, D. W. (1978). A disaggregation and thin section analysis of the size and mass distribution of the chondrules in the bjurbîŠŤe and chainpur meteorites, *Earth and Planetary Science Letters* 38(2): 391 – 400.
URL: *http://www.sciencedirect.com/science/article/pii/0012821X78901139*

Iida, A., Nakamoto, T., Susa, H. & Nakagawa, Y. (2001). A shock heating model for chondrule formation in a protoplanetary disk, *Icarus* 153: 430–450.

Jones, R. H., Lee, T., Jr., H. C. C., Love, S. G. & Shang, H. (2000). *Formation of chondrules and CAIs: Theory vs. observation*, Protostars and Planets IV, Univ. of Arizona Press, Tucson, pp. 927–962.

Jones, R. H. & Lofgren, G. E. (1993). A comparison of feo-rich, porphyritic olivine chondrules in unequilibrated chondrites and experimental analogues, *Meteoritics* 28: 213–221.

Kadono, T. & Arakawa, M. (2005). Breakup of liquids by high velocity flow and size distribution of chondrules, *Icarus* 173: 295–299.

Kadono, T., Arakawa, M. & Kouchi, A. (2008). Size distributions of chondrules and dispersed droplets caused by liquid breakup: An application to shock wave conditions in the solar nebula, *Icarus* 197: 621–626.

Kato, T., Nakamoto, T. & Miura, H. (2006). Maximal size of chondrules in shock wave heating model: Stripping of liquid surface in a hypersonic rarefied gas flow, *Meteorit. Planet. Sci.* 41: 49–65.

Landau, L. D. & Lifshitz, E. M. (1987). *Fluid Mechanics, Course of Theoretical Physics*, Vol. 6, 2nd edn, Elsevier/Butterworth/Heinemann, Oxford, UK.

Lofgren, G. & Russell, W. J. (1986). Dynamic crystallization of chondrule melts of porphyritic and radial pyroxene composition, *Geochim. Cosmochim. Acta* 50: 1715–1726.

Miura, H. & Nakamoto, T. (2006). Shock-wave heating model for chondrule formation: Prevention of isotopic fractionation, *Astrophys. J.* 651: 1272–1295.

Miura, H. & Nakamoto, T. (2007). Shock-wave heating model for chondrule formation: Hydrodynamic simulation of molten droplets exposed to gas flows, *Icarus* 188: 246–265.

Miura, H., Nakamoto, T. & Doi, M. (2008). Origin of three-dimensional shapes of chondrules. i: Hydrodynamics simulations of rotating droplet exposed to high-velocity rarefied gas flow, *Icarus* 197: 269–281.

Miura, H., Nakamoto, T. & Susa, H. (2002). A shock-wave heating model for chondrule formation: Effects of evaporation and gas flows on silicate particles, *Icarus* 160: 258–270.

Miura, H., Yasuda, S. & Nakamoto, T. (2008). Fragment-collision model for compound chondrule formation: Estimation of collision probability, *Icarus* 194: 811–821.

Morris, M. A. & Desch, S. J. (2010). Thermal histories of chondrules in solar nebula shocks, *Astrophys. J.* 722: 1474–1494.

Morris, M. A., Desch, S. J. & Ciesla, F. J. (2009). Cooling of dense gas by h_2o line emission and an assessment of its effects in chondrule-forming shocks, *Astrophys. J.* 691: 320–331.

Nagashima, K., Tsukamoto, K., Satoh, H., Kobatake, H. & Dold, P. (2006). Reproduction of chondrules from levitated, hypercooled melts, *J. Crys. Growth* 293: 193–197.

Nakagawa, Y., Sekiya, M. & Hayashi, C. (1986). Settling and growth of dust particles in a laminar phase of a low-mass solar nebula, *Icarus* 67: 375–390.

Nakamura, T., Tanaka, R., Yabe, T. & Takizawa, K. (2001). Exactly conservative semi-lagrangian scheme for multi-dimensional hyperbolic equations with directional splitting technique, *Journal of Computational Physics* 174(1): 171 – 207.
URL: *http://www.sciencedirect.com/science/article/pii/S0021999101968883*

Nelson, L. S., Blander, M., Skaggs, S. R. & Keil, K. (1972). Use of a co_2 laser to prepare chondrule-like spherules from supercooled molten oxide and silicate droplets, *Earth Planet. Sci. Lett.* 14: 338–344.

Nelson, V. E. & Rubin, A. E. (2002). Size-frequency distributions of chondrules and chondrule fragments in ll3 chondrites: Implications for parent-body fragmentation of chondrules, *Meteorit. Planet. Sci.* 37: 1361–1376.

Radomsky, P. M. & Hewins, R. H. (1990). Formation conditions of pyroxene-olivine and magnesian olivine chondrules, *Geochim. Cosmochim. Acta* 54: 3475–3490.

Rubin, A. E. (1989). Size-frequency distributions of chondrules in co3 chondrites, *Meteoritics* 24: 179–189.

Rubin, A. E. & Grossman, J. N. (1987). Size-frequency-distributions of eh3 chondrules, *Meteoritics* 22: 237–251.

Rubin, A. E. & Keil, K. (1984). Size-distributions of chondrule types in the inman and allan hills a77011 l3 chondrites, *Meteoritics* 19: 135–143.

Ruzmaikina, T. V. & Ip, W. H. (1994). Chondrule formation in radiative shock, *Icarus* 112: 430–447.

Sekiya, M. & Nakamura, T. (1996). Condition for the formation of the compound chondrules in the solar nebula, *Proc. NIPR Symp. Antarct. Meteorites* 9: 208–217.

Sekiya, M., Uesugi, M. & Nakamoto, T. (2003). Flow in a liquid sphere moving with a hypersonic velocity in a rarefied gas—an analytic solution of linearized equations, *Prog. Theor. Phys.* 109: 717–728.

Srivastava, A., Inatomi, Y., Tsukamoto, K., Maki, T. & Miura, H. (2010). In situ visualization of crystallization inside high temperature silicate melts, *J. Appl. Phys.* 107: 114907.

Susa, H. & Nakamoto, T. (2002). On the maximal size of chondrules in shock wave heating model, *Astrophys. J.* 564: L57–L60.

Teitler, S. A., Paque, J. M., Cuzzi, J. N. & Hogan, R. C. (2010). Statistical tests of chondrule sorting, *Meteorit. Planet. Sci.* .

Tsuchiyama, A. & Nagahara, H. (1981-12). Effects of precooling thermal history and cooling rate on the texture of chondrules: A preliminary report, *Memoirs of National Institute of Polar Research. Special issue* 20: 175–192.
URL: *http://ci.nii.ac.jp/naid/110000009441/*

Tsuchiyama, A., Nagahara, H. & Kushiro, I. (1980). Experimental reproduction of textures of chondrules, *Earth Planet. Sci. Lett.* 48: 155–165.

Tsuchiyama, A., Osada, Y., Nakano, T. & Uesugi, K. (2004). Experimental reproduction of classic barred olivine chondrules: Open-system behavior of chondrule formation, *Geochim. Cosmochim. Acta* 68: 653–672.

Tsuchiyama, A., Shigeyoshi, R., Kawabata, T., Nakano, T., Uesugi, K. & Shirono, S. (2003). Three-dimensional structures of chondrules and their high-speed rotation, *Lunar Planet. Sci.* 34: 1271–1272.

Tsukamoto, K., Satoh, H., Takamura, Y. & Kuribayashi, K. (1999). A new approach for the formation of olivine-chondrules by aero-acoustic levitation, *Antarct. Meteorites* 24: 179–181.

Uesugi, M., Akaki, T., Sekiya, M. & Nakamura, T. (2005). Motion of iron sulfide inclusions inside a shock-melted chondrule, *Meteorit. Planet. Sci.* 40: 1103–1114.

Uesugi, M., Sekiya, M. & Nakamoto, T. (2003). Deformation and internal flow of a chondrule-precursor molten sphere in a shocked nebular gas, *Earth Planets Space* 55: 493–507.

Wasson, J. T., Alexander, N. K., Lee, M. S. & Rubin, A. E. (1995). Compound chondrules, *Geochim. Cosmochim. Acta* 59: 1847–1869.

Wood, J. A. (1984). On the formation of meteoritic chondrules by aerodynamic drag heating in the solar nebula, *Earth Planet. Sci. Lett.* 70: 11–26.

Xiao, F., Yabe, T. & Ito, T. (1996). Constructing oscillation preventing scheme for advection eqution by rational function, *Comp. Phys. Comm.* 93: 1–12.

Yabe, T. & Aoki, T. (1991). A universal solver for hyperbolic equations by cubic-polynomial interpolation i. one-dimensional solver, *Comp. Phys. Comm.* 66: 219–232.

Yabe, T. & Wang, P. Y. (1991). Unified numerical procedure for compressible and incompressible fluid, *J. Phys. Soc. Jpn.* 60: 2105–2108.

Yabe, T., Xiao, F. & Utsumi, T. (2001). The constrained interpolation profile method for multiphase analysis., *J. Comp. Phys.* 169: 556–593.

Yasuda, S., Miura, H. & Nakamoto, T. (2009). Compound chondrule formation in the shock-wave heating model: Three-dimensional hydrodynamics simulation of the disruption of a partially-molten dust particle, *Icarus* 204: 303–315.

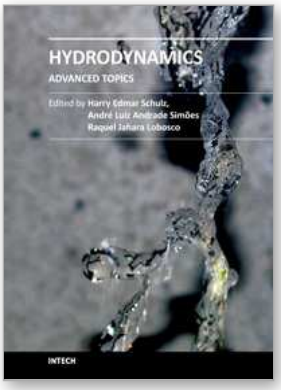

Hydrodynamics - Advanced Topics

Edited by Prof. Harry Schulz

ISBN 978-953-307-596-9
Hard cover, 442 pages
Publisher InTech
Published online 22, December, 2011
Published in print edition December, 2011

The phenomena related to the flow of fluids are generally complex, and difficult to quantify. New approaches - considering points of view still not explored - may introduce useful tools in the study of Hydrodynamics and the related transport phenomena. The details of the flows and the properties of the fluids must be considered on a very small scale perspective. Consequently, new concepts and tools are generated to better describe the fluids and their properties. This volume presents conclusions about advanced topics of calculated and observed flows. It contains eighteen chapters, organized in five sections: 1) Mathematical Models in Fluid Mechanics, 2) Biological Applications and Biohydrodynamics, 3) Detailed Experimental Analyses of Fluids and Flows, 4) Radiation-, Electro-, Magnetohydrodynamics, and Magnetorheology, 5) Special Topics on Simulations and Experimental Data. These chapters present new points of view about methods and tools used in Hydrodynamics.

INTECH
open science | open minds

InTech Europe
University Campus STeP Ri
Slavka Krautzeka 83/A
51000 Rijeka, Croatia
Phone: +385 (51) 770 447
Fax: +385 (51) 686 166
www.intechopen.com

InTech China
Unit 405, Office Block, Hotel Equatorial Shanghai
No.65, Yan An Road (West), Shanghai, 200040, China
中国上海市延安西路65号上海国际贵都大饭店办公楼405单元
Phone: +86-21-62489820
Fax: +86-21-62489821